Structure and Evolution of Hurricane Claudette on 7 September 1991 from Airborne Doppler Radar Observations. Part II: Thermodynamics

NICOLAS VILTARD

Centre d'Étude des Environnements Terrestre et Planétaires, CNRS—Université Versailles Saint-Quentin, Vélizy, France

FRANK ROUX

Laboratoire d'Aérologie, CNRS—Université Paul Sabatier, Toulouse, France

(Manuscript received 30 May 1996, in final form 29 April 1997)

ABSTRACT

In Part I, the kinematic and precipitating fields of Hurricane Claudette have been analyzed, using airborne Doppler radar data collected on 7 September 1991 by the two National Oceanic and Atmospheric Administration (NOAA) WP-3D research aircraft. Evidence of an incipient ''eyewall replacement cycle'' and its influence on Hurricane Claudette circulation have been revealed through the EVTD (extended velocity track display) method. This study has been conducted for six successive analyses in a domain of 200 km × 200 km × 12 km domain from 1700 to 2200 UTC.

A thermodynamic retrieval method is adapted here to the EVTD geometry to deduce the temperature and pressure perturbation fields from the previously EVTD-derived wind fields. The relation between the evolution of the circulation and the thermodynamic structure of Hurricane Claudette can now be studied. The main feature deduced from this method is a positive temperature perturbation about 8–9 K warmer than the environment at the center of the storm circulation, associated with a pressure deficit of about 25 hPa at the sea level. During the considered period, the temperature perturbation maximum changed according to the evolution of the inner eyewall, while warming in the middle part was related to intensifying external outward motions and cooling in the outer part, due to stronger inflow. Meanwhile, there is no distinct evolution of the pressure perturbation field. Comparisons between the retrieved thermodynamic fields and in situ data collected by both aircraft along their flight track show qualitatively good agreement, although the EVTD-retrieved values have substantially lower amplitudes, probably due to the strong spatial and temporal filtering. Analyses of fields with different time filtering confirms that inertia–gravity waves that may propagate outward from the system do not seem to affect the retrieved kinematic and thermodynamic fields.

Considering only the symmetric part (wavenumber 0) of this EVTD kinematic and thermodynamic description of Hurricane Claudette, the authors have verified that throughout most of the considered domain of the study, gradient wind balance, hydrostatic equilibrium, and thermal wind relation are nearly verified. Nevertheless, there are some indications that supergradient winds may be found locally in the lower inner part of the eyewall.

1. Introduction

In Part I of this study (Roux and Viltard 1995), the extended velocity track display (EVTD) method (Roux and Marks 1996) was applied to airborne Doppler radar data collected in Hurricane Claudette on 7 September 1991 during a research flight conducted by the National Oceanic and Atmospheric Administration's (NOAA) Hurricane Research Division (HRD, Miami, Florida) with two WP-3D aircraft. In this approach, the tangential, radial, and vertical components of the wind velocity relative to the storm motion, as well as the precipitating water content, are expressed in a cylindrical coordinate system using a Fourier series truncated at wavenumber 2 in azimuth. Combined with an efficient filtering of the small-scale and transient motions, this method allows analyses of the ''mesoscale'' kinematics structure and the ''slow'' evolution of the storm, through six ''snapshots'' at hourly intervals from 1700 to 2200 (all times are UTC).

These results showed that, during the period under consideration, the storm experienced a partial replacement of the inner eyewall by an external one (Shapiro and Willoughby 1982; Willoughby et al. 1982; Willoughby 1990a). This evolution clearly appeared in the reflectivity composites from both the horizontally scanning C-band lower fuselage (LF) and the vertically scanning X-band tail Doppler (TA) radars. A crescent-shaped zone of initially high reflectivity values progressively shrank and diminished, while at a larger radius strong echoes formed an increasingly organized ring of intense precipitation. The flow fields deduced from the Doppler data showed coherent features. The

Corresponding author address: Dr. Nicolas Viltard, CETP, 10-12 avenue de l'Europe, 78140 Vélizy, France.
E-mail: nicolas.viltard@cetp.ipsl.fr

tangential wind maximum associated with the inner eyewall weakened throughout the six sequences, while a secondary maximum at larger radii strengthened. The low-level inflow that initially reached the inner part of the storm and fed the inner eyewall's updraft region was progressively diverted into a newly formed updraft circlosed by the outer zone of high reflectivity.

Here, we use slightly different wind fields with respect to those presented in Part I: a constraint is added in the function F to be minimized in order to deduce the tangential and radial wind components [(10) in Part I]. This constraint forces the radial and tangential components to vanish at the center ($r = 0$) of the storm. Only minor modifications of the wind field result from this change, and the discussion of its structure and evolution in Part I remains valid. But this change is necessary to retrieve reliable thermodynamic fields near the storm center. Another important point concerns time filtering. In the analysis of the streamfunction representing the secondary circulation, some uncertainties appear between the ''slow'' evolution of vortex structure and convection or convectively induced inertia–gravity waves. In section 3, we will present a series of tests to address this question.

Beyond this analysis of the precipitation and kinematic structure and evolution of the storm, we present here results from a thermodynamic retrieval method that allows to calculate the corresponding temperature and pressure fields. These thermodynamic fields are calculated using the same decomposition in Fourier series as in Part I. Such an analysis allows to explicitly separate each variable as a sum of symmetric and asymmetric parts, and to study their relative roles. To our knowledge, this is the first time such a retrieval (which has been extensively used for ground-based and airborne Doppler radar data) has been applied to airborne Doppler radar data in hurricane, although Gamache et al. (1993) implicitly resolved the temperature field in their analysis of the water budget of Hurricane Norbert (1984).

The thermodynamic structure of hurricanes is relatively well understood. Since the 1960s, many in situ observations have been collected during flights by NOAA and U.S. Air Force aircraft into hurricanes and typhoons. Combinations of flight-level and dropsonde data obtained during multiple airborne penetrations of the inner core region of hurricanes provide extensive information on the three-dimensional structure of pressure and temperature. Nevertheless, these studies suffer two limitations. First, as data from successive trajectories at different track angles across the storm circulation center are combined to obtain an azimuthal description, little information can be deduced on the evolution during the considered period. By carefully maintaining a single flight level, Willoughby et al. (1982) and Willoughby (1990a) were, however, able to observe some changes of the wind and mass fields. Second, the description is obviously limited to the highest level the aircraft can fly and provides no data from 6 km to the top of hurricane circulation near or above the tropopause level (≈15 km).

Through the analysis of in situ data, Jordan and Jordan (1954), and Jordan (1958) remarked that the warm anomaly in the inner core of tropical cyclones is maximum in the mid- to upper troposphere. LaSeur and Hawkins (1963), and Hawkins and Rubsam (1968) found a 16-K positive anomaly between 7 and 10 km in Hurricane Cleo (1958) and Hurricane Hilda (1964), respectively. Hawkins and Imbembo (1976) showed the presence of two temperature maxima of about 9 K at 4- and 10-km altitude within the eye of Hurricane Inez (1966). All of these authors found that the largest horizontal temperature gradients occur in the eyewall. Hawkins and Rubsam (1968), and Hawkins and Imbembo (1976) have shown that the temperature perturbations are nearly constant in the low levels, close to the sea surface.

In section 2, we adapt a thermodynamic retrieval method (Roux et al. 1993) to EVTD-derived wind and precipitation fields. In section 3, the results obtained are presented and compared with independent flight-level measurements of temperature and pressure. In section 4, we address balance of the symmetric vortex. After a brief review of the thermal wind equation and some considerations on the time filtering, a balanced symmetric vortex is deduced from the analysis. Section 5 contains conclusions and perspectives.

2. Thermodynamic retrieval adapted to EVTD

As explained in Part I, the tangential V_T, radial V_R, and vertical W components of the wind vector, as well as the precipitating water content q_p, are analyzed as truncated Fourier series in 50 rings of 2-km width, extending from 1- to 99-km radius around the circulation center and 25 levels of 500-m depth from 0.5- to 12.5-km altitude. These components are expressed as

$$V_T = \sum_{m=0}^{4} p(m)T_m, \tag{1a}$$

$$V_R = \sum_{m=0}^{4} p(m)R_m, \tag{1b}$$

$$W = \sum_{m=0}^{4} p(m)W_m, \tag{1c}$$

$$q_p = \sum_{m=0}^{4} p(m)q_m, \tag{1d}$$

where $p(0) = 1$, $p(1) = \cos\varphi$, $p(2) = \sin\varphi$, $p(3) = \cos(2\varphi)$, and $p(4) = \sin(2\varphi)$, where φ is the storm-relative azimuth relative to circulation center (φ is equal to 0° in the eastern direction and 90° in the northern direction).

In a first step, all the thermodynamic variables are considered as the sum of an environmental part (subscript e) and a perturbation term (subscript d). Then, following this notation, the equation of motion with respect to a hydrostatic reference state is

$$\frac{\partial \mathbf{V}}{\partial t} + (\mathbf{V}\cdot\boldsymbol{\nabla})\mathbf{V} = -C_p\theta_{ve}\boldsymbol{\nabla}\pi_d + g\left(\frac{\theta_{cd}}{\theta_e} - q_p\right)\mathbf{k} - 2\boldsymbol{\Omega}\times\mathbf{V}, \tag{2}$$

where $\mathbf{V}$ is the velocity vector, C_p is the specific heat at constant pressure, θ_e and θ_{ve} are the potential and virtual potential temperature in the environment, respectively. Here, $\pi = (P/1000\ \text{hPa})^{R/C_p}$ is the Exner function, g is the gravity acceleration, $\mathbf{\Omega}$ is the earth's rotation vector (whose components are 0 in the west–east direction), j is in the south–north direction, and f is in the vertical. Here, θ_{cd} is the virtual cloud potential temperature perturbation defined as

$$\theta_{cd} = \theta_d + (0.61q_{vd} - q_c)\theta_e, \tag{3}$$

where θ_d is the potential temperature perturbation, q_{vd} is the water vapor perturbation term, and q_c is the nonprecipitating cloud water content. Here, (2) is expressed in a cylindrical coordinate system relative to the storm circulation center. The coordinate system is then moving with the storm, and height is the vertical coordinate. The temperature θ_{cd} and pressure π_d perturbations in (2) are to be written as truncated Fourier series similar to (1a), (1b), (1c), and (1d):

$$\theta_{cd} = \sum_{m=0}^{4} p(m)\theta_{cdm} \tag{4a}$$

$$\pi_d = \sum_{m=0}^{4} p(m)\pi_{dm}. \tag{4b}$$

Then, for each of the wavenumber components $m = 0$–4, equations for the radial, vertical, and azimuthal pressure gradients can be deduced as, respectively,

$$\frac{\partial \pi_{dm}}{\partial r} = A_{rm}, \tag{5a}$$

$$\frac{\partial \pi_{dm}}{\partial z} = A_{zm} + \frac{g}{C_p\theta_{ve}\theta_e}\theta_{cdm}, \tag{5b}$$

$$\frac{\sigma_m}{r}\pi_{dm} = A_{\varphi m'}, \tag{5c}$$

where r is the radius from the circulation center, z is the altitude above the sea level, and $\sigma_m = \{0, -1, 1, -2, 2\}$, $m' = \{0, 2, 1, 4, 3\}$ for $m = \{0, 1, 2, 3, 4\}$, respectively. Here, (5c) results from the presence of azimuth φ only in $p(m)$, in (4a) and (4b) [that means there is no $m = 0$ realization of (5c)]. The A_{rm}, A_{zm}, and $A_{\varphi m'}$ terms are normalized accelerations in the radial, tangential, and vertical direction, respectively. Note that, owing to the strong time filtering (discussed in Part I), the local time changes are much smaller than the advective terms and are not taken into account in (5a), (5b), and (5c).

The radial, tangential, and vertical pressure perturbation gradients are calculated from the velocity components and precipitating water contents developed through (1a), (1b), (1c), (1d), and the environmental data as

$$\begin{aligned} A_r &= \frac{-1}{C_p\theta_{ve}\theta_e}\left[V_R\frac{\partial V_R}{\partial r} + \frac{1}{r}V_T\frac{\partial V_R}{\partial \varphi} + W\frac{\partial V_R}{\partial z} - V_T\left(f + \frac{V_T}{r}\right) - jW\cos\varphi\right] \\ &= \frac{-1}{C_p\theta_{ve}}\left\{\begin{array}{l} \displaystyle\sum_{m=0}^{4} p(m)R_m \sum_{m=0}^{4} p(m)\frac{\partial R_m}{\partial r} + \frac{1}{r}\sum_{m=0}^{4} p(m)T_m \sum_{m=0}^{4} \sigma(m')p(m')R_{m'} \\ \quad + \displaystyle\sum_{m=0}^{4} p(m)W_m \sum_{m=0}^{4} p(m)\frac{\partial R_m}{\partial z} - \sum_{m=0}^{4} p(m)T_m\left[f + \frac{1}{r}\sum_{m=0}^{4} p(m)T_m\right] \\ \quad - j\displaystyle\sum_{m=0}^{4} p(m)W_m\cos(\varphi) \end{array}\right\} \\ &= \sum_{m=0}^{8} p(m)A_{rm}, \end{aligned} \tag{6a}$$

$$\begin{aligned} A_\varphi &= \frac{-1}{C_p\theta_{ve}}\left[V_R\frac{\partial V_T}{\partial r} + \frac{V_T\partial V_T}{r\ \partial\varphi} + W\frac{\partial V_T}{\partial z} + V_R\left(f + \frac{V_T}{r}\right) - jW\sin\varphi\right] \\ &= \sum_{m=0}^{8} p(m)A_{\varphi m}, \end{aligned} \tag{6b}$$

$$\begin{aligned} A_z &= \frac{-1}{C_p\theta_{ve}}\left[V_R\frac{\partial W}{\partial r} + \frac{V_T}{r}\frac{\partial W}{\partial \varphi} + W\frac{\partial W}{\partial z} + j(V_T\sin\varphi - V_R\cos\varphi)\right] \\ &= \sum_{m=0}^{8} p(m)A_{zm}. \end{aligned} \tag{6c}$$

Calculating ∂(5a)/∂z $-$ ∂(5b)/∂r and ∂(5c)/∂z $-$ ∂(5b)/$\partial\varphi$ gives equations for the components of vorticity which can be expressed as functions of the radial, B_{rm} ($m = 0$–4), and azimuthal, $B_{\varphi m'}$, of each of the spectral components of virtual cloud potential temperature perturbation. We have

$$\frac{\partial\theta_{cdm}}{\partial r} = B_{rm}, \tag{7a}$$

$$\frac{\sigma_m}{r}\theta_{cdm} = B_{\varphi m'}. \tag{7b}$$

The values of σ_m and m' for $m = 0$–4 are similar to those given above. The coefficients B_{rm} and $B_{\varphi m'}$ are derived from (6a), (6b), and (6c) as

$$B_r = \frac{C_p\theta_{ve}\theta_e}{g}\left\{\frac{\partial}{\partial z}\left[\sum_{m=0}^{8} p(m)A_{rm}\right] - \frac{\partial}{\partial r}\left[\sum_{m=0}^{8} p(m)A_{zm}\right]\right\} = \sum_{m=0}^{8} p(m)B_{rm}, \tag{8a}$$

$$B_\varphi = \frac{C_p\theta_{ve}\theta_e}{g}\left\{\frac{\partial}{\partial z}\left[\sum_{m=0}^{8} p(m)A_{\varphi m}\right] - \frac{1}{r}\frac{\partial}{\partial\varphi}\left[\sum_{m=0}^{8} p(m)A_{zm}\right]\right\} = \sum_{m=0}^{8} p(m)B_{\varphi m}. \tag{8b}$$

In order to obtain a description of the pressure and temperature perturbation fields coherent with that of the wind components and precipitating water contents, which are limited to wavenumber 2, the Fourier series in (4a) and (4b) are truncated at wavenumber 2. Then, only the part of (6a), (6b), (6c), (8a), and (8b) for $m < 4$ will be taken into account in the following.

As shown by Roux (1985), the inclusion of thermodynamic equation in the retrieval scheme is necessary to deduce the three-dimensional structure of θ_{cd}. In cylindrical coordinates, and supposing that the time derivative is smaller than the other ones, the thermodynamic equation may be written as

$$V_R\frac{\partial\theta_{cd}}{\partial r} + \frac{V_T}{r}\frac{\partial\theta_{cd}}{\partial\varphi} + W\frac{\partial\theta_{cd}}{\partial z} - \nabla(\kappa_T\nabla\theta_{cd}) = B_T, \tag{9}$$

where B_T is the heat source–sink term, and κ_T is the thermodynamic eddy diffusion coefficient calculated as in Smagorinski (1963). Following Roux et al. (1993), B_T is

$$B_T = B_{T0} + \delta_S(B^S_{T1} + \beta\theta_{cd}) + (1 - \delta_S)B^{NS}_{T1}, \tag{10a}$$

where

$$B_{T0} = W\left(-0.61\theta_e\frac{dq_{ve}}{dz} - \frac{d\theta_e}{dz}\right) - \frac{L_f}{C_p\pi_e}M, \tag{10b}$$

$$B^S_{T1} = W\left(1.61\theta_e\frac{L_{v/s}}{C_p\pi_e}\right)\gamma_e + \theta_e F(q_p), \tag{10c}$$

$$B^{NS}_{T1} = W\left(\frac{L_{v/s}}{C_p\pi_e} - 0.61\theta_e\right)F(q_p), \tag{10d}$$

where q_{ve} is the water vapor content of environment, $F(q_p)$ is the production rate of precipitation, L_f and $L_{v/s}$ are latent heat of fusion and vaporization/sublimation, respectively. The coefficient M is the melting rate parametrized as Leary and Houze (1979). The coefficient γ_e is the vertical gradient of water content for a wet adiabat passing through (θ_e, π_e), the linearization of which gives a value for β [more details can be found in Roux et al. (1993)]. The coefficient δ_S is 1 in saturated air and 0 in unsaturated air.

Adaptation of (9) to the EVTD approach is obtained by developing the different variables as truncated Fourier series. The melting rate and the production rate of precipitation are deduced from the precipitating water contents (Roux 1985). Note also that the saturation state (δ_s) is determined from the only symmetric ($m = 0$) part of $F(q_p)$ applied to all the wavenumber components ($m = 0$–4). As a matter of fact, it would be meaningless to consider that a given region is saturated for one wavenumber, while unsaturated for another one. Moreover, it has to be emphasized that the values of $F(q_p)$ associated with wavenumbers ($m > 0$) are much smaller than those given by the symmetric part ($m = 0$). The right-hand side of (9), truncated at wavenumber 2, can therefore be written as

$$B_T = \sum_{m=0}^{4} p(m)B_{Tm}. \tag{11}$$

The left-hand side of (9) is a sum of products of Fourier series, so, it can be expressed as a Fourier series. Hence, (9) becomes

$$\sum_{m=0}^{4} p(m)\left(\sum_{n=0}^{4} a_{mn}\theta_{cdn} + b_{mn}\frac{\partial\theta_{cdn}}{\partial r} + c_{mn}\frac{\partial\theta_{cdn}}{\partial z}\right) = \sum_{m=0}^{4} p(m)B_{Tm}, \tag{12}$$

where a_{mn}, b_{mn}, and c_{mn} result from products of the Fourier series associated with the velocity components V_T, V_R, W, the virtual cloud potential temperature perturbation θ_{cd}, and from derivatives of Fourier series associated with θ_{cd} in the azimuthal direction.

An important characteristic of (12) is that all the coefficients (θ_{cdn}, $n = 0$–4) of the Fourier series for the temperature perturbation are to be considered for each coefficient of the Fourier series for B_T. In other words, the thermodynamic equation (9) can be used to complement (2), provided that all the orders ($m = 0$–4) are simultaneously retrieved. Therefore, the function to be minimized to solve θ_{cdm} for $m = 0$–4 and for N_R rings and N_Z levels may be written as

$$F = \sum_{\substack{i=1,N_R \\ k=1,N_Z}} \sum_{m=0}^{4} \left\{ \left(\frac{\partial \theta_{cdm}}{\partial r} - B_{rm} \right)^2 + \left(\frac{1}{r}\theta_{cdm} - \sigma_m B_{\varphi m'} \right)^2 + \left[\sum_{n=0}^{4} \left(a_{mn}\theta_{cdn} + b_{mn}\frac{\partial \theta_{cdn}}{\partial r} + c_{mn}\frac{\partial \theta_{cdn}}{\partial z} \right) - B_{Tm} \right]^2 + \underbrace{\upsilon[\partial^2(\theta_{cdm})]^2}_{\text{a}} \right\}, \tag{13}$$

where term ''a'' is added to minimize the second-order radial and vertical derivatives of θ_{cdm}, to be coherent with Part I [see (10)] so as to avoid spatial discontinuities between the different rings and levels.

As discussed in Roux (1985), only relative temperature perturbation with respect to an unknown constant can be deduced from (13). In the present case, a unique constant of 4 K is added to the temperature perturbation retrieved for all the analyses in order to obtain positive (i.e., warmer than the environment) values everywhere in the considered domain.

Retrieval of the pressure perturbation field is relatively more simple as each order is independent of the others. Hence, the function to be minimized to solve π_{dm} for $m = 0$–4 and for each N_R rings and N_Z levels may be written as

$$G = \sum_{\substack{i=1,N_R \\ k=1,N_Z}} \sum_{m=0}^{4} \left[\left(\frac{\partial \pi_{dm}}{\partial r} - A_{rm} \right)^2 + \left(\frac{1}{r}\pi_{dm} - \sigma_m A_{\varphi m'} \right)^2 + \left(\frac{\partial \pi_{dm}}{\partial z} - A_{zm} - \frac{g}{C_p \theta_{ve} \theta_e}\theta_{cdm} \right)^2 \right]. \tag{14}$$

As for (13), an additional constraint on radial and vertical secondary derivative is used to control the continuity of the field from one ring and/or level to the other.

Likewise, a −15-hPa constant is added to the pressure perturbation retrieved for all analyses in order to obtain negative values (pressure deficit) everywhere in the considered domain. It is important to note that these temperature and pressure constants are rather arbitrary, leading to relative θ_{cd} and π_d values. Actual perturbations with respect to the environmental characteristics may be somewhat larger.

3. Retrieved thermodynamic structure

All the retrieved thermodynamic fields discussed below have been obtained from fields of wind components and precipitating water content slightly different from those presented in Part I. The main difference between the old and the new wind analyses is that a constraint has been added to ensure that the wind components are zero at the circulation center ($r = 0$).

The new T_0 field (wavenumber 0—symmetric—component of the tangential wind) and the mass-flow streamfunction (deduced from the wavenumber, 0 components of the radial and vertical wind: $\partial\psi/\partial z = -2\pi\rho r R_0$ and $\partial\psi/\partial r = 2\pi\rho r W_0$) are shown in Fig. 1, comparable with the Figs. 8 and 9 in Part I. The symmetric tangential wind field is very similar. The radial flow shows the same general characteristics, with a main inflow below the 7-km altitude and an outflow above. This structure of the vertical circulation is simple at 1700. The main updraft lies at 10–30 km and there is a weak downdraft at about 35-km, both associated with the low levels inflow. From 1800 to 2200, this structure evolves considerably. It has to be noted that the chosen time filtering (discussed in Part I) ensures a good coherence of the evolution of the different features from one analysis to the next. First a couplet of up draft (at 45–50-km radius) and downdraft (at 75 km) develops and intensifies at 1900. At this time, a third structure (counterclockwise gyre) centered at 8-km altitude and 35-km radius appears. At 2000, this gyre strengthens, isolating the initial inner gyre from the strong outer one that has developed at 1800. Then at 2100 and 2200, the weaker inner clockwise gyre moves upward, while the intermediate counterclockwise gyre, centered at 2.5-km altitude and 25-km radius at 2200, reinforces, maintaining a strong updraft at about 30- to 70-km radii. The external clockwise gyre remains stable as it moves slowly outward from 65-km radius at 2100 to 75 km at 2200. This evolution may be related to the formation and intensification of the new eyewall, while the older one progressively decreases and moves inward and upward. This phenomenon will be discussed in the following section.

a. Symmetric fields

The evolution of the symmetric temperature perturbation field, that is, the wavenumber $m = 0$ component of θ_{cd}, is shown in Fig. 2. This figure reveals two phases

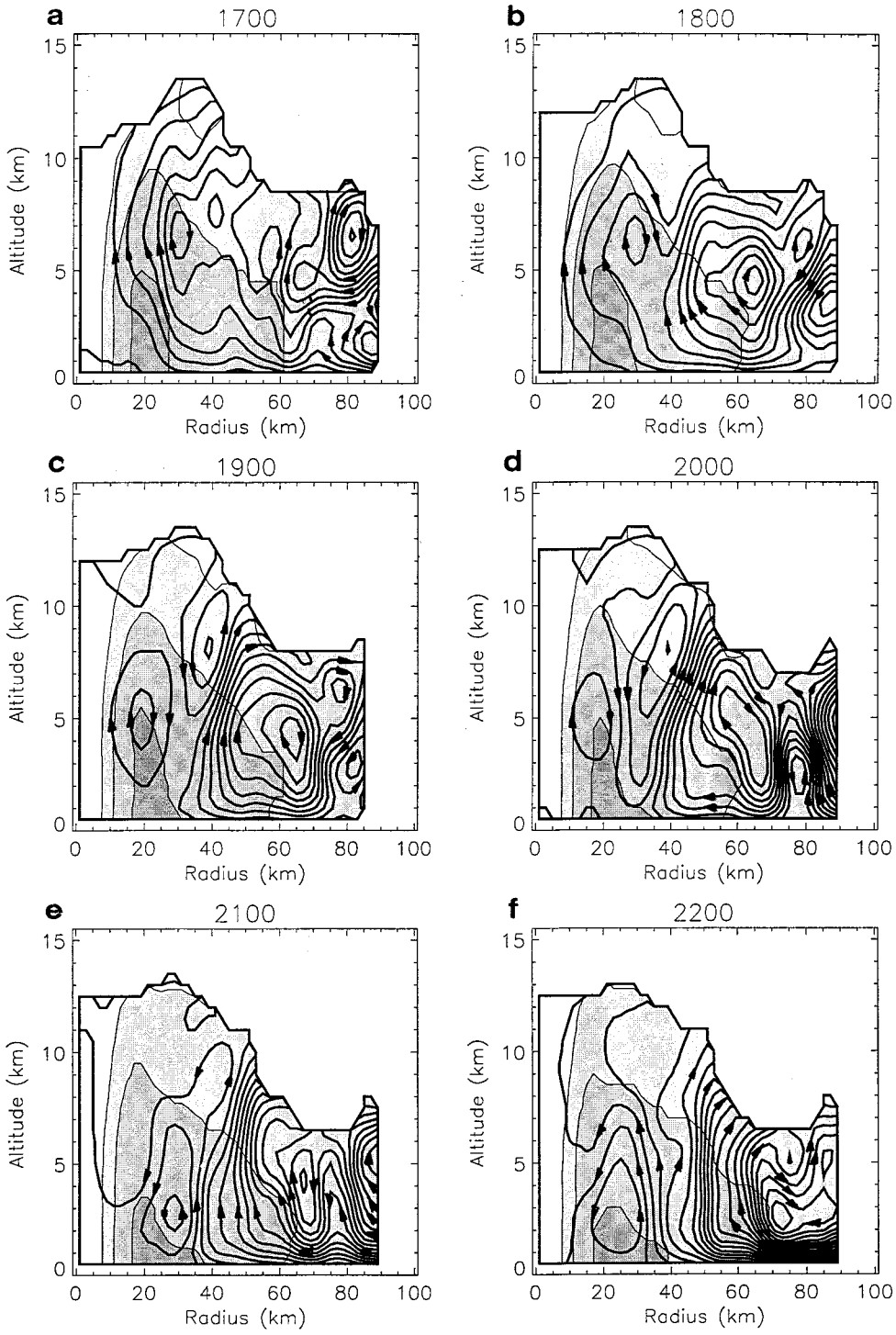

FIG. 1. Radius–height cross section of the symmetric EVTD-derived tangential velocity (m s^{-1}) depicted by increasing shades of gray for thresholds of 20, 30, and 40 m s^{-1}. The oriented contours (arrows) denote the streamfunction for the secondary symmetric circulation (contour every $0.2 \times 10^{+9}$ kg s^{-1}). The different panels refer to successive times of analysis: (a) 1700, (b) 1800, (c) 1900, (d) 2000, (e) 2100, and (f) 2200.

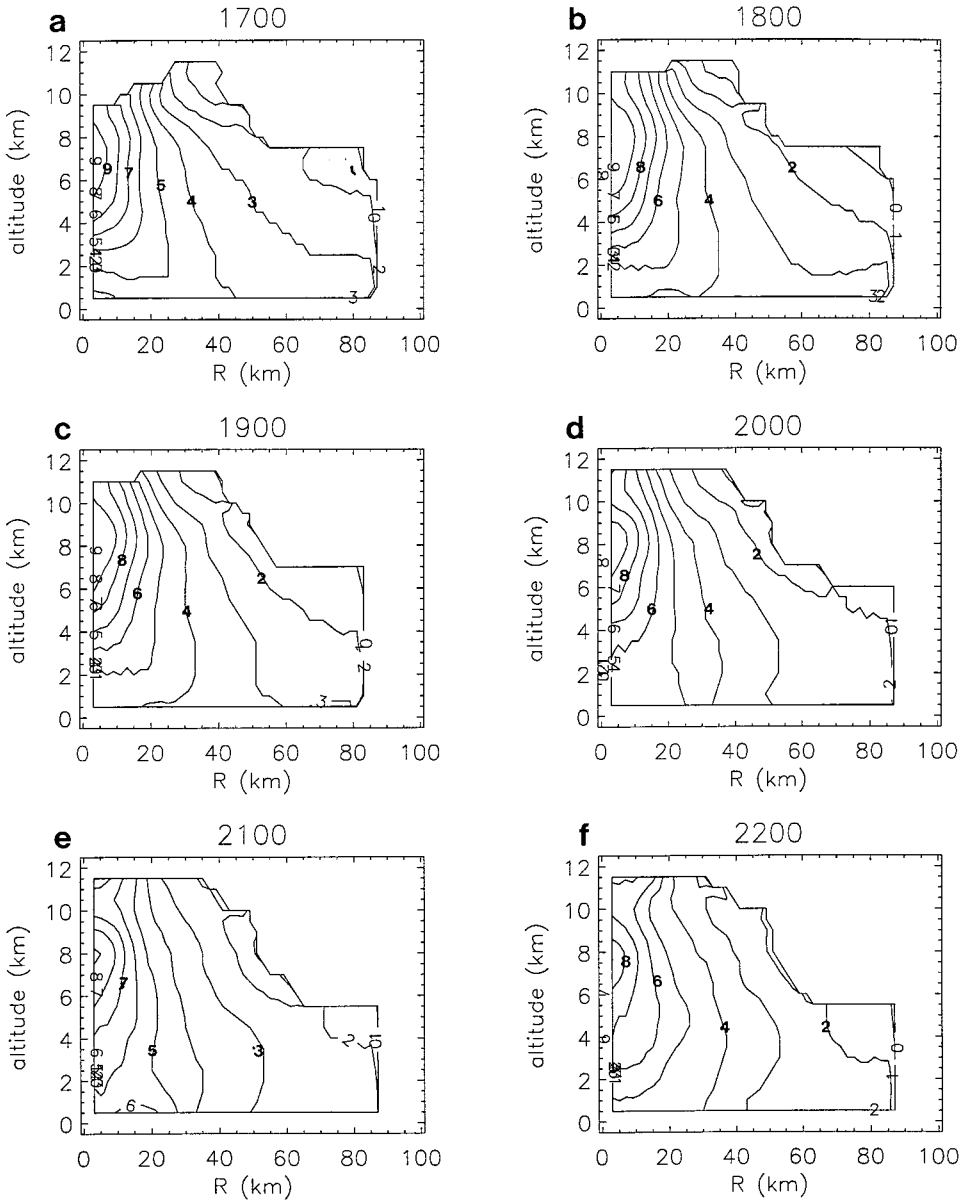

FIG. 2. Radius–height cross section of the symmetric part of the retrieved temperature perturbation (contour interval is 1 K).

in the evolution of the thermodynamic structure. The first one from 1700 to 1900 shows, at the center of the storm, a slight increase of the maximum at a progressively higher level. At 7-km radius, the largest retrieved temperature perturbations are 9.1 K at 7-km altitude at 1700, 10.8 K at 7.5 km at 1800, and 10.4 K at 8.2 km at 1900. During the second phase (same radius), θ_{cd} progressively decreases in the inner part of the storm, with maximum values of 9.5 K at 8-km altitude at 2000, 9.2 K at 8 km at 2100, and 8.6 K at 7.5 km at 2200. At 2100 and 2200, a secondary maximum with θ_{cd} greater than 7 K appears above 11-km altitude. Meanwhile, noticeable changes occur in the middle part of the domain (40 km $< r <$ 60 km). At 50-km radius, the 3-K isotherm shows a distinct bulge between 1.5- and 4-km altitude at 2000 that extends between 1 and 4.5 km at 2100 and between 2 and 5 km at 2200. Changes are also observed at higher levels at 10-km altitude: 3-K isotherm expands radially from 25-km radius at 2000, to 28 km at 2100, and 30 km at 2200. Throughout the whole period, the external part of the domain experiences a significant cooling. At radii greater than 70 km, the 3-K isotherm decreases from 2- to below 1-km altitude from 1700 till 1900, and the 2-K isotherm decreases from 4.5- to 3-km altitude from 2000 to 2200.

This observed thermodynamic evolution can be

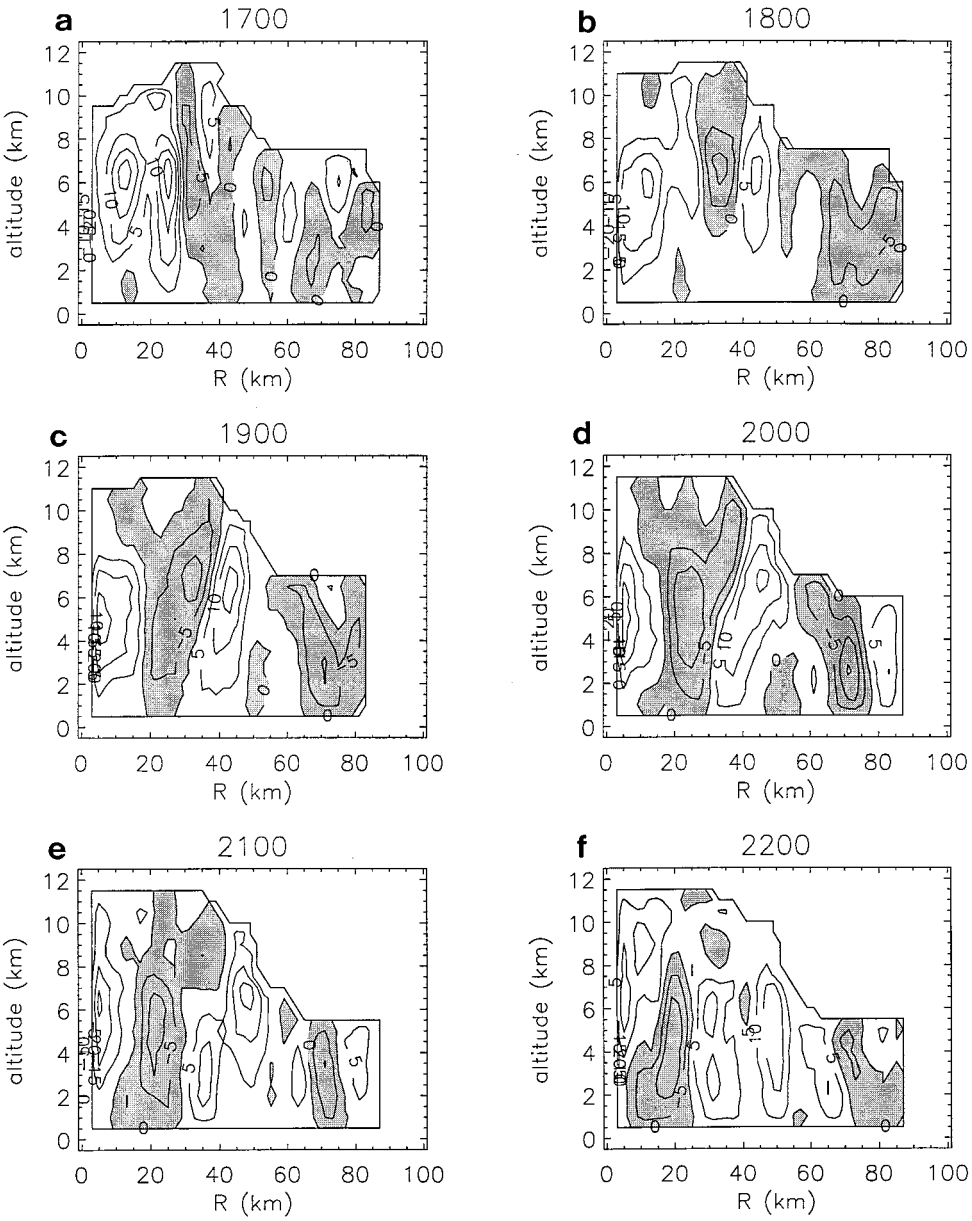

FIG. 3. As in Fig. 2 except for the symmetric part of the diagnosed heat source/sink (contour interval is 5 K h^{-1}, shaded zone are for negative values).

linked to the changes in the secondary circulation, as discussed in Part I and displayed Fig. 1. Concerning the inner part of the storm, the slight warming observed during the first phase is related to the upward circulation in the initial inner eyewall. During the second phase, the associated decrease of temperature perturbation occurs when the above-mentioned inner updraft progressively disappears. In the middle part of the domain the observed changes in θ_{cd}, first, at midlevels after 2000 are linked to the strengthening of the updraft zone, and second, at lowlevels the cooling on the external part is probably due to the stronger inflow of external air.

A comparison of Figs. 1 and 2, shows that the largest vertical shear of tangential velocity and radial gradient of temperature perturbation are found in the region between 10- and 20-km radii. This supports the hypothesis by Willoughby (1990b, 1991) from the analysis of flight-level data, that the gradient wind balance describes the azimuthally averaged swirling wind and its tendency in the inner core region (radii less than 150 km) of mature hurricanes.

Figure 3 displays the symmetric part of heat source–sink term $S(T)$ calculated from the retrieved temperature perturbation field [through $(\mathbf{V}\cdot\nabla)\theta_{cd} + Wd\theta_e/dz$]. Its structure and evolution are strongly correlated with that of W_0 (Fig. 9 in Part I, and Fig. 1 here). It may be seen

that, at 1700, two main heat sources (each 15 K h^{-1}) are located at 6-km altitude, 15- and 25-km radii, respectively. A radial alternation of secondary (± 5 K h^{-1}) heat sources and sinks extends in the external part of the domain. This structure evolves from 1800 to 2200. First, the main heat source (at 6-km altitude and 15-km radius at 1700) moves progressively inward to 7-km radius. At the same time, as the other largest heat source observed at 1700 vanishes, a source–sink pair centered at 40-km radius and 7-km altitude strengthens. This feature moves progressively inward to 30-km radius at 2000. Then it remains at the same radius till 2200, but its altitude decreases (from 7 km to 4–5 km) between 2000 to 2200. Finally, in the external part of the domain (radius greater than 60 km), other source–sink pairs alternatively appear and vanishe during the six analyses. Modification in the spatial distribution of the $S(T)$ term is probably due to that of the secondary circulation (Fig. 1), as heat sources and sinks are linked to upward and downward motions.

It is important to note that these heat source–sink terms are nearly balanced by the cooling–warming induced by the associated upward–downward motions, which implies too weak a net heating to explain the retrieved radial temperature gradients. Hence, other physical processes are necessarily involved in the thermodynamic equilibrium of hurricane core region.

A radius–height cross section of the retrieved pressure perturbation field is shown in Fig. 4. The maximum relative pressure perturbation (pressure deficit) is about -25 hPa at surface level (1 km). The three-dimensional pressure field (not presented) is quite symmetric, strongly dominated by wavenumber 0. This retrieved pressure perturbation does not evolve very much during the six analyses and results mainly from the hydrostatic effect due to the presence of warmer air above, with the maximum depression at the center of the storm.

b. Three-dimensional fields

Once the components of θ_{cd} and π_d are retrieved from (13) and (14), three-dimensional Cartesian fields with a horizontal grid spacing of 2 km are reconstructed. Due to the spectral truncation, spatial resolution is poorer in the external part of the domain than it is close to the center of the storm. For this reason, the three-dimensional field of temperature perturbation is calculated only in a subdomain 100 km $\times$ 100 km $\times$ 12 km.

At 3-km altitude (Fig. 5), the structure of the temperature perturbation field evolves with time. At 1700 and 1800, an asymmetric maximum (6–7 K) is located in the northern and inner part of the eyewall (radius less than 20 km). At 1900 and 2000, the largest temperature perturbations move westward and are slightly weaker with a maximum of about 6 K. At 2100 and 2200, the temperature maximum (6 K) extends to the south-southeastern part of the domain. The other isotherms (3 and 4 K) are mostly symmetric and do not change very much during the successive analyses.

At 6-km altitude (Fig. 6), the temperature perturbations are stronger than in the lower levels. At 1700 and 1800, a maximum of about 9 K is located in the northeastern and inner part of the eyewall (radius less than 15 km). At 1900 and 2000, the maximum (9 K) remains nearly at the same place but it occupies a smaller area. At 2100 and 2200, the maximum temperature perturbation weakened progressively to 8 K and moves slightly to the north. As for 3-km altitude, the structure at radii greater than 20 km is much more symmetric.

At 9-km altitude (Fig. 7) the asymmetry is more pronounced than in the lower levels. This can clearly be seen, throughout the period, as elliptic isotherms extending in the south–north direction. The evolution of the maximum in the core is also different with an east–west asymmetry at radii smaller than 15 km. Early on, this maximum of 9 K is located close to the circulation center, in the southeastern part of the domain at 1700, and its area is greatest at 1800 and 1900 with a larger extent in the eastern part. At 2000 and 2100, it is only a small spot in the eastern part of the domain. At 2200, the maximum is only 8 K as the final temperature field is the more asymmetric.

The general structure and evolution of the three-dimensional temperature perturbation field agree with that of the wind field. The asymmetries in the temperature perturbations are likely associated with induced subsidence at the lower level and injection of warm updraft air at the upper level. In one hand, comparisons between Fig. 5 and 12 in Part I show some correlation between the $\theta_{cd} > 6$ K values and the downward motions associated with the inner eyewall circulation in the northern then west to southwestern quadrants. The lack of subsidence in the outer rings may explain the more symmetric contours at larger radii. On the other hand, the more and more pronounced asymmetry observed in Fig. 7 can be related to the developing updraft in the southern quadrant.

c. Comparison with in situ data

During the flight, both aircraft collected in situ measurements of pressure and temperature. The data from successive radial penetrations of the storm and six circles around the inner eyewall (cf. Table 1, in Part I) can be used for comparisons with the retrieved values. To allow this comparison, the in situ data are low-pass filtered to eliminate wavelengths smaller than 7 km along the flight track, using a Cressman (1959) filter. These filtered data have the same spectral characteristics as the retrieved values. One should, however, note that the flight-level data are filtered only along the flight track, while EVTD-derived values are subject to strong radial, azimuthal, and temporal filtering (more details can be found in Part I).

Also, the aircraft altitude is not exactly constant and

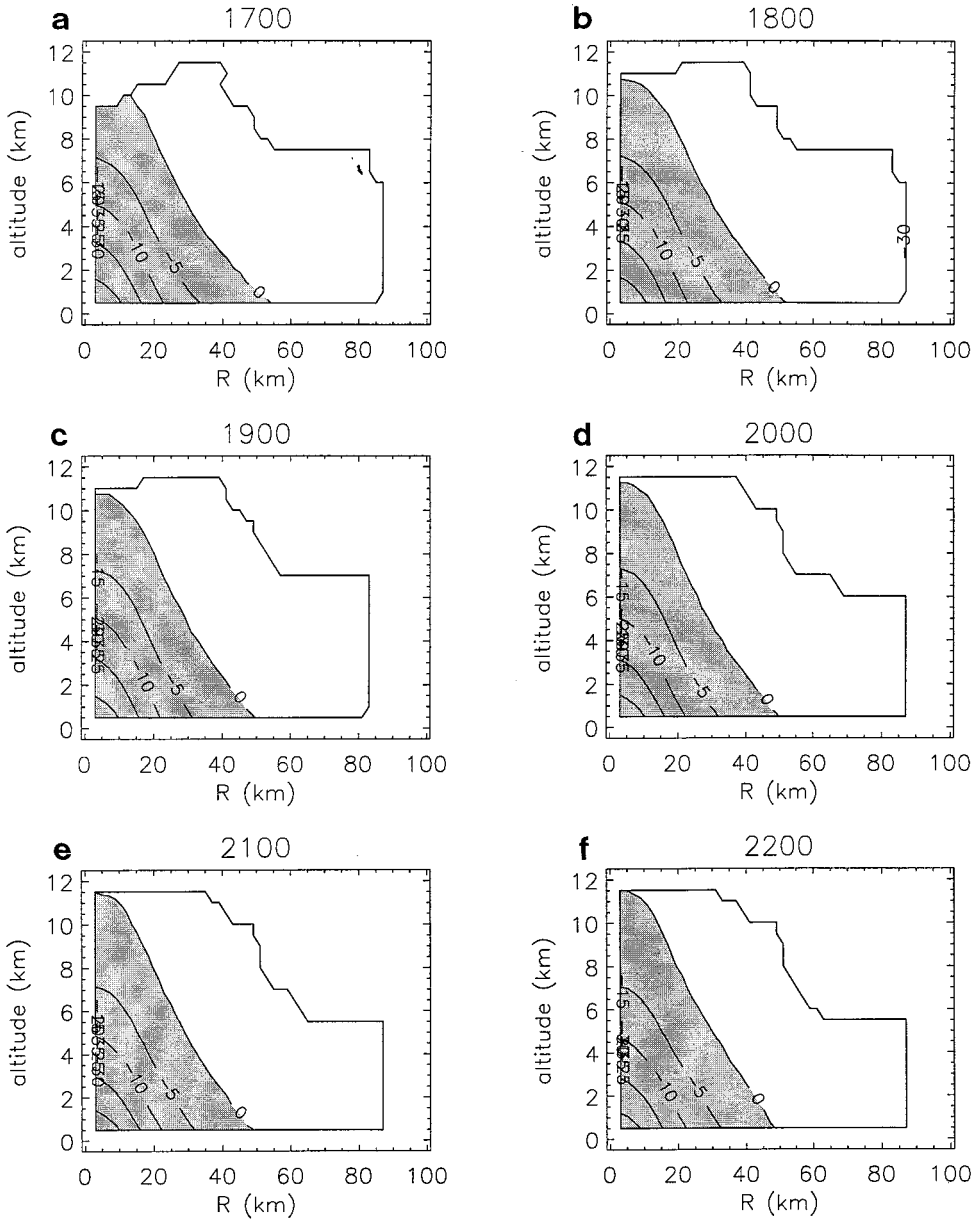

FIG. 4. As in Fig. 2 except for the symmetric part of the retrieved pressure perturbation (contour interval is 5 hPa).

often differs from the levels where the pressure and temperature perturbations are retrieved. Hence, a correction is applied on both the temperature and pressure in situ data, using the standard atmosphere, to deduce equivalent values at altitudes of 2.5 km for *N42RF* and 3.5 km for *N43RF*. The comparisons presented here are for legs 3 (south–north), 5 (east–west), and 8 (northeast–southwest) for *P3-42* (Fig. 8), and legs 8 (southeast–northwest) and circles 1–2 and 5–6 for *P3-43* (Fig. 9). Note that the in situ data collected during the circles flown by *N43RF* around the storm circulation center provides information on the azimuthal variation, which are not easily available from the traditional radial legs.

A comparison between the flight-level data collected with the two aircraft, while they were flying at the same altitude and location with a time shift of about 15 min during the ferry between Bermuda and Hurricane Claudette, reveals that *N43RF* temperatures have a systematic bias of 1.4 K warmer than those of *N42RF*. This bias has been taken into account in the present analysis.

A difficult problem is navigation of the aircraft in the domain because the position of the circulation center is only approximate, due to both the geometry and the composition of the different legs used in the EVTD analysis (see also Part I). We assume that the aircraft flew exactly across the circulation center on each leg

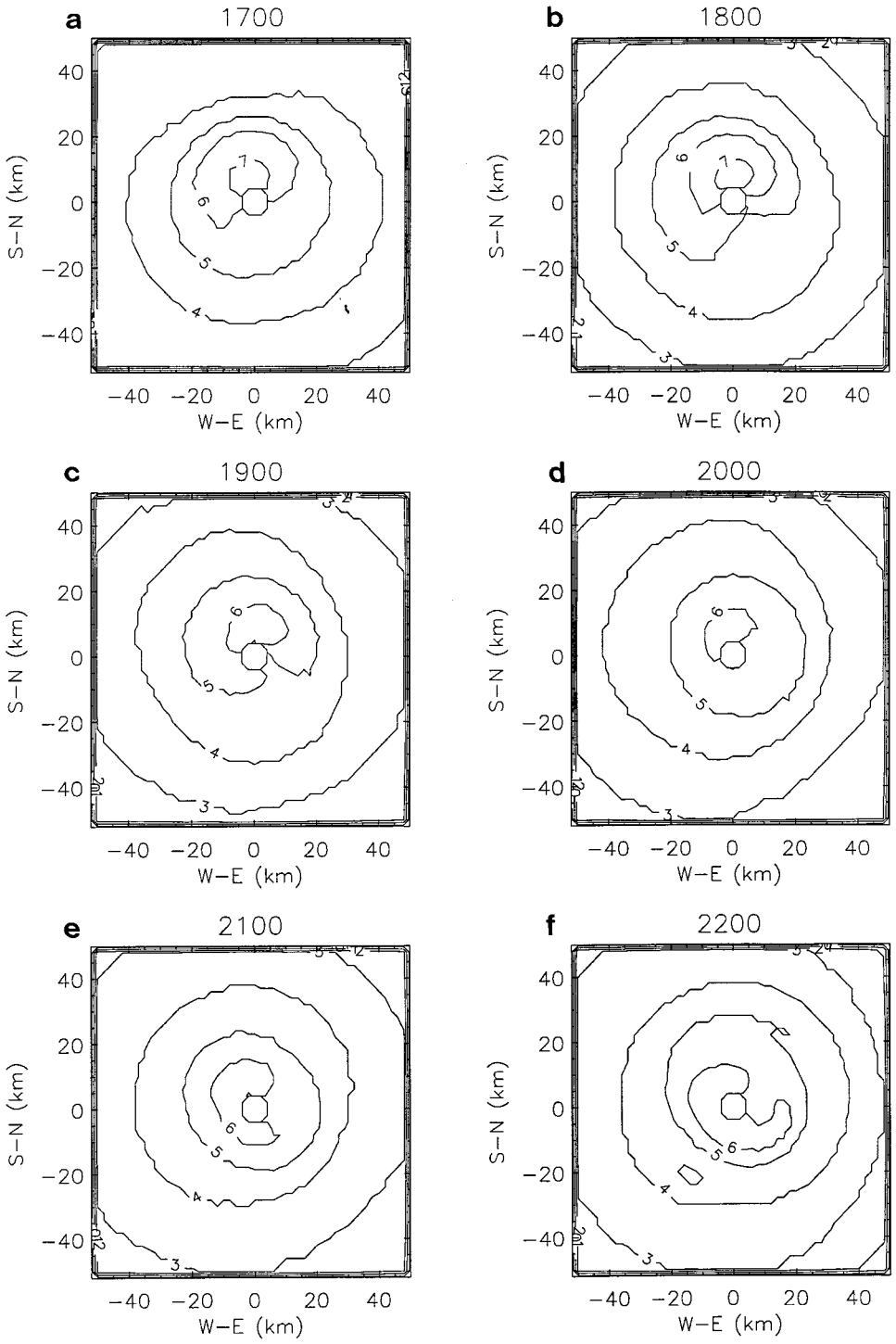

FIG. 5. Horizontal cross section (100 km × 100 km domain) at 3-km altitude for retrieved temperature perturbation (contour interval is 1 K).

(except for the circles) and that the position of the center is given by the minimum of flight-level pressure. For the circular trajectories flown with *N43RF*, we take the corresponding circulation center position given by *N42RF*, corrected from the mean propagation of the Hurricane Claudette (4.6 m s^{-1} from 152°).

The temperature perturbations displayed in the left-hand side of Figs. 8 and 9 are similar, with maximum

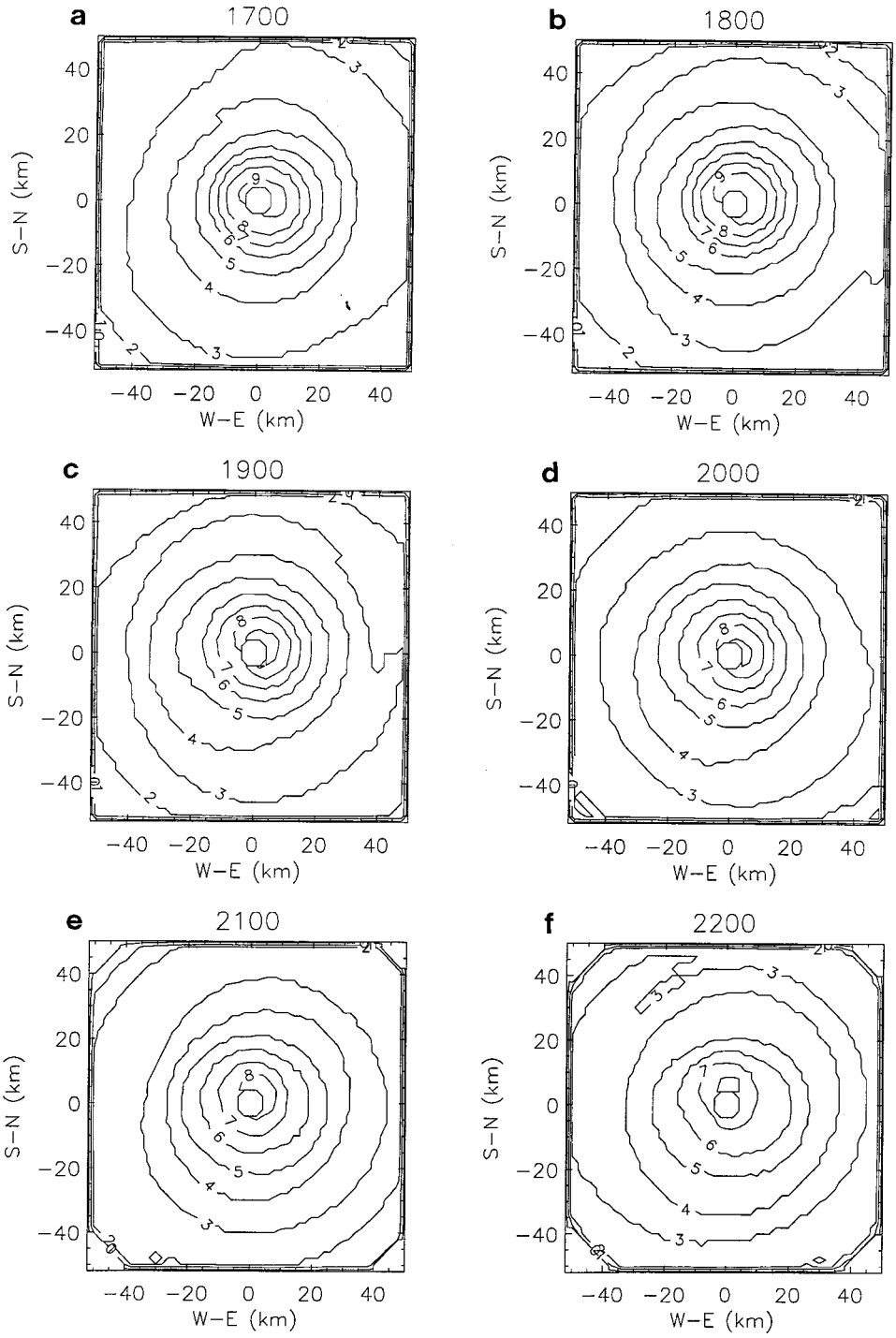

FIG. 6. As in Fig. 5 except for 6-km altitude.

positive perturbations in the eye. Not surprisingly, the retrieved temperature values shows less intense maximum and smoother variations than the flight-level data. The mean values and the standard deviations for the in situ data are about twice as large as the EVTD-retrieved values, although their rms differences remain relatively small (Table 1). This difference certainly results from the lack of radar data in the precipitation-free region inside the inner eyewall, and also the strong radial, azimuthal, and temporal filtering used to ensure that all the small-scale convective and inertial perturbations are eliminated in the EVTD-derived field (see Part I). Nev-

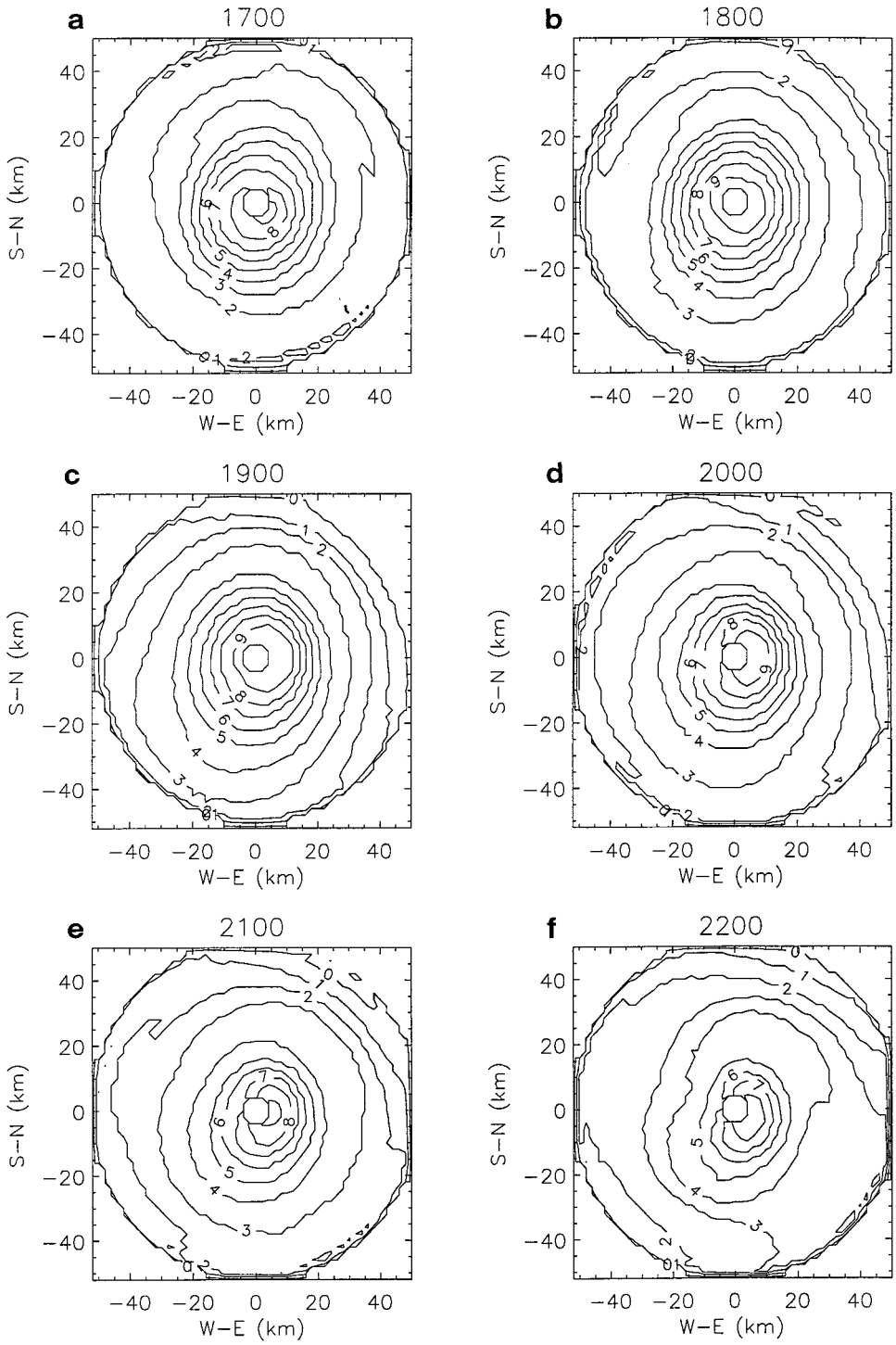

FIG. 7. As in Fig. 5 except for 9-km altitude.

ertheless, the asymmetric structure of the temperature in situ measurements is rather correctly described by the EVTD-retrieved temperature values, except maybe for leg 8 of *N42RF* (Fig. 8e), for which the EVTD maximum is on the opposite side of the eye as compared to the in situ data. The comparison of the two circles (Fig. 9a,b) of *N43RF* gives a good idea of how correctly the azimuthal asymmetries are reproduced in the EVTD-retrieved values.

The retrieved and measured pressure perturbations (right-hand side of Figs. 8 and 9) are similar, except for the circular legs 1 + 2 and 5 + 6 for *N43RF*. It has to

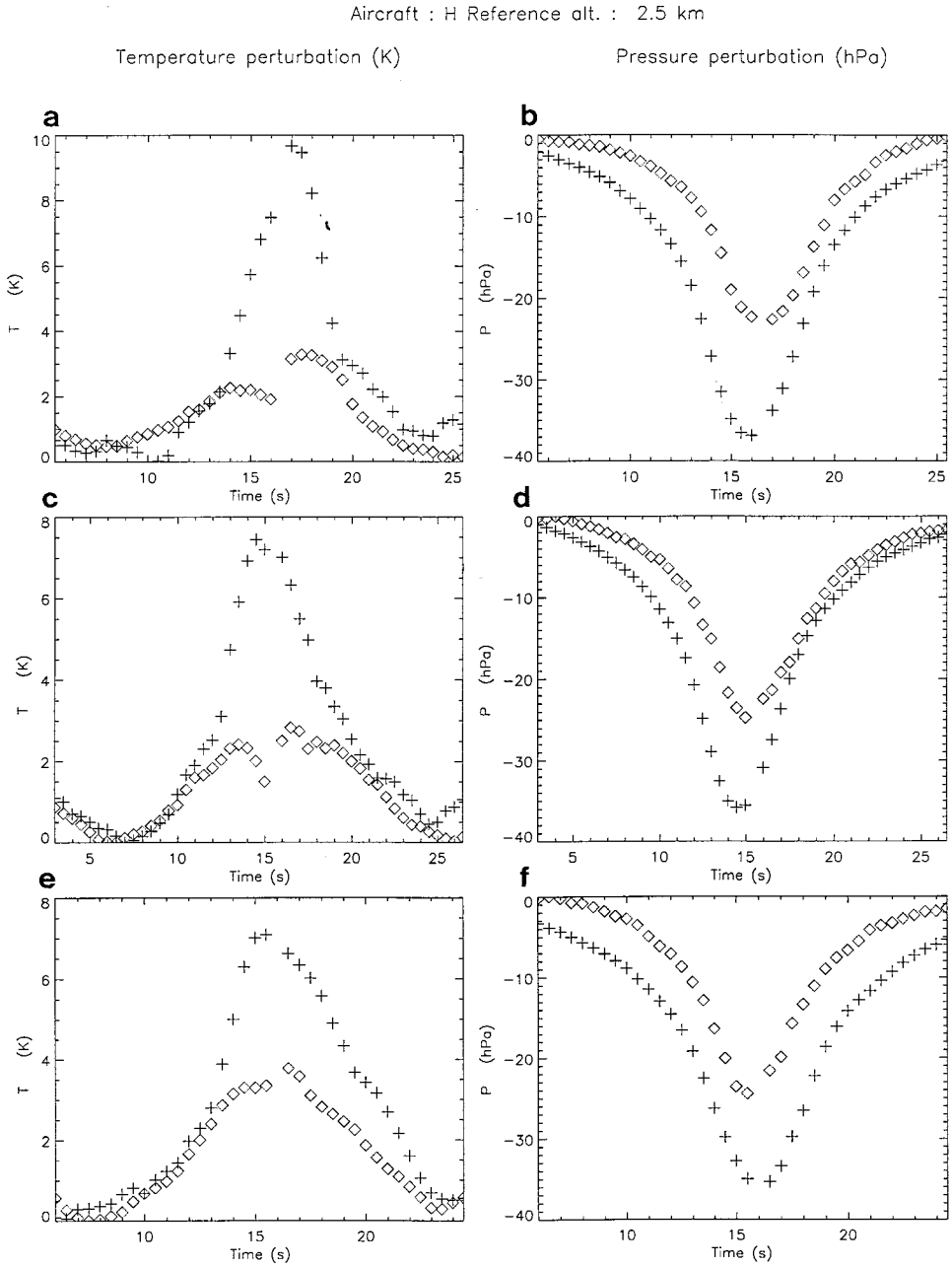

FIG. 8. Comparison of the retrieved values and the flight-level measurements for *N42RF*'s leg 3 [(a) and (b)], 5 [(c) and (d)], and 8 [(e) and (f)]. Left-hand side is for temperature perturbations (K), right-hand side for pressure perturbations (hPa). Leg numbers refer to Table 1 in Part I. Diamond signs stands for the EVTD-retrieved values, plus signs for the in situ measurements.

be pointed out that this difference between radial and circular legs is emphasized by a different ordinate scale from 0 to −40 hPa for the former and from 0 to −12 hPa for the latter. The difference for the circular legs is more a difference about the structure: position of the maxima and the minima. The poor quality of these last comparisons (Figs. 9b,d) can be due to uncertainties in the exact location of the storm circulation center, as the horizontal pressure gradient is very strong at a radial distance of about 25 km from the center where the circular legs were flown.

These comparisons show that the EVTD-retrieved thermodynamic fields are fairly coherent with the in situ data, even if they are smoother, due to the filtering of the wind fields. One important point is to verify that these thermodynamic perturbations agree with the EVTD-derived wind field and if there exists a relationship between the radial gradient of the symmetric tem-

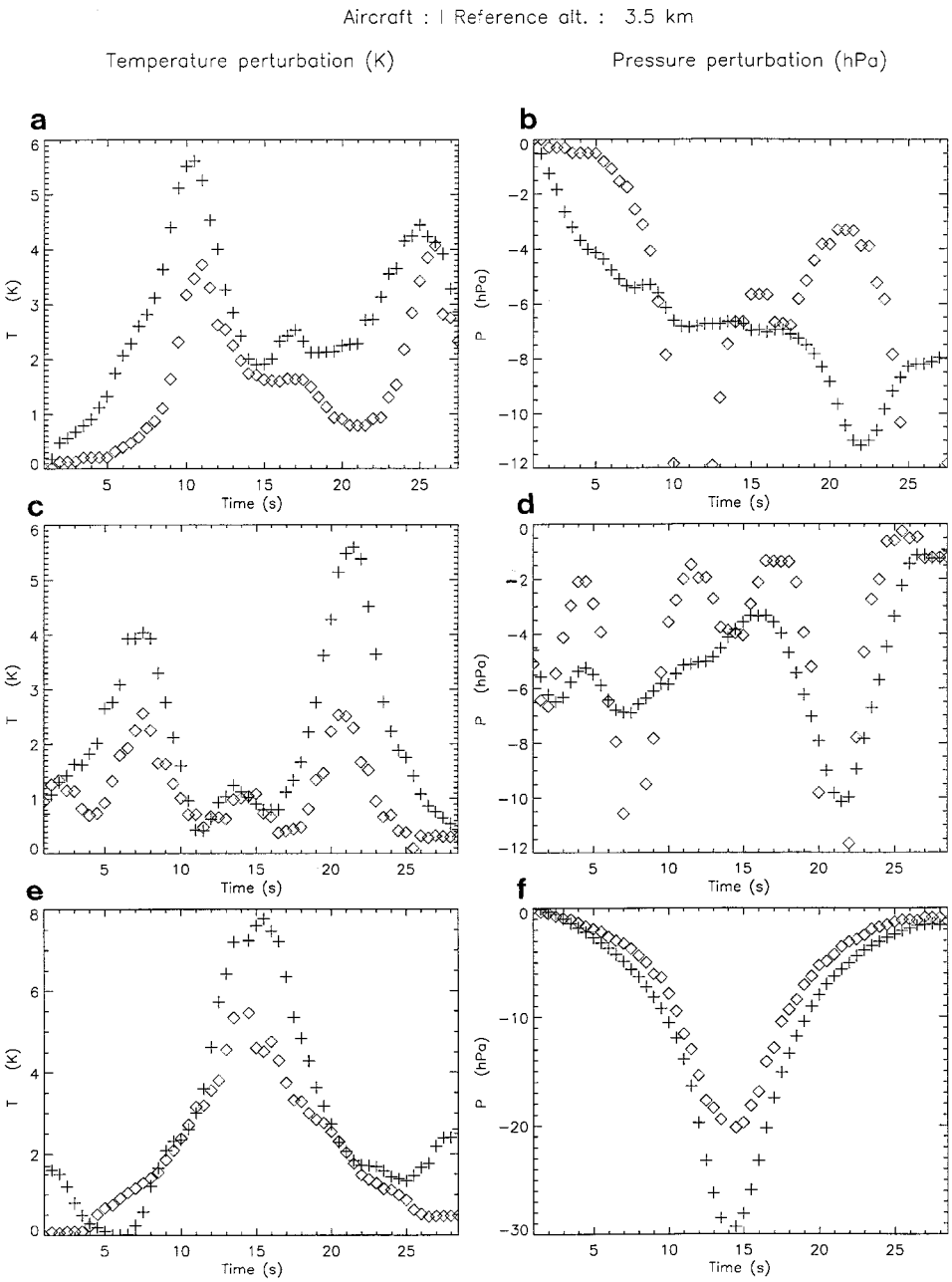

FIG. 9. As in Fig. 8 except for *N43RF*'s leg 8 (a)–(b), circles 1–2 (c)–(d), and circles 5–6 (e)–(f).

perature perturbation and the vertical shear of the symmetric tangential velocity. In order to answer this question, the following section compares theoretical hypotheses with the kinematic and thermodynamic description retrieved from the EVTD analysis of the radar data. One has to keep in mind that the thermodynamic and kinematic fields obtained in the present study are in a general balance, due to the variational method used to calculate the thermodynamic variables from the wind field. Nevertheless, the balance we want to verify in the following is much more restrictive than those induced by the numerical resolution of the thermodynamic variable using primitive equations, such as the equation of motion and the thermodynamic equation.

4. Gradient wind balance

a. Thermal wind equation

Shapiro and Willoughby (1982) have proposed an analysis of the hurricane inner core dynamics using a separation of each variable in their symmetric and asymmetric

TABLE 1. Comparison between the pressure and temperature perturbations retrieved from the EVTD analyses and the in situ data. The legs and circles number for each aircraft refer to Part I, Table 1.

	N42RF (≈2.5 km)			*N43RF* (≈3.6 km)		
	Leg 3	Leg 5	Leg 8	Leg 8	Circles 1 + 2	Circles 5 + 6
Temperature						
Mean EVTD (K)	1.3	1.1	1.5	1.9	1.5	1.0
Mean in situ (K)	2.4	2.2	2.5	2.7	2.7	2.0
std dev EVTD (K)	1.0	0.9	1.2	1.5	1.1	0.7
std dev in situ (K)	2.6	2.1	2.3	2.2	1.3	1.5
rms difference (K)	1.9	1.5	1.2	1.1	0.8	1.0
Pressure						
Mean EVTD (hPa)	−6.8	−7.5	−7.3	−6.0	−6.4	−4.4
Mean in situ (hPa)	−13.2	−11.6	−14.5	−8.5	−6.7	−5.1
std dev EVTD (hPa)	7.2	7.2	7.1	6.0	4.9	3.8
std dev in situ (hPa)	10.8	10.3	9.8	8.4	2.5	2.3
rms difference (hPa)	4.3	3.9	3.0	2.4	4.4	2.4

parts: $X = X_S + X_A$. The expansion in truncated Fourier series used in the EVTD analysis offers a natural way to separate the symmetric part and asymmetric part as

$$X_S = X_0, \tag{15}$$

$$X_A = \sum_{m=1}^{4} p(m)X_m. \tag{16}$$

Using this formalism, the equation of motion, the thermodynamic equation, and the airmass conservation equation can be decomposed into symmetric and asymmetric parts. Here, as Shapiro and Willoughby (1982), we only discuss the results relative to the symmetric part, which largely dominates the dynamic and thermodynamic structure of mature tropical cyclones like Claudette.

The symmetric part of the radial component of the equation of motion becomes

$$T_0\left(f + \frac{T_0}{r}\right) = -\frac{\partial\Phi_0}{\partial r}, \tag{17}$$

with Φ_0, the symmetric geopotential defined as $d\Phi_0 = -C_p\theta_{ve}d\pi$.

The hydrostatic equilibrium for symmetric circulation can be written as

$$g\frac{\theta_{cd0}}{\theta_{ve}} = -\frac{\partial\Phi_0}{\partial z}. \tag{18}$$

Partial differentation of (17) with respect to *z*, and (18) with respect to *r*, gives the thermal wind relation for the symmetric secondary circulation:

$$\xi S = \frac{g}{\theta_{ve}}\frac{\partial\theta_{cd0}}{\partial r}, \tag{19}$$

where $\xi = [2(T_0/r) + f]$ is the inertia parameter, $S = \partial T_0/\partial z$ is the vertical shear of tangential wind, and we define $\beta^2 = \xi S$ as the baroclinicity. Equation (19) expresses an equilibrium between the horizontal temperature gradient and the vertical shear of the tangential wind. This is a strong constraint on the storm dynamics. In the major part of the troposphere, the inertia parameter ξ is positive because of the cyclonic circulation. The decreasing values of the tangential wind with altitude lead to negative values for the vertical wind shear *S*. Hence, the left-hand side of (19) is negative almost everywhere, and θ_{cd0} is a decreasing function of radius *r*. Moreover, this equation predicts that the radial gradients of θ_{cd0} will be larger in the eyewall, where the vertical shear of tangential wind is stronger. Such a feature can be seen through a comparison of Figs. 1 and 2.

b. Influence of time filtering

In order to check the quality of the EVTD-derived kinematic and thermodynamic fields, we have made some tests about the time filtering. One important problem is to distinguish the proper slow [*O*(1 h)] evolution of the system from the possible influence of propagating inertia-gravity waves and convection (Willoughby 1977) and to evaluate the impact of these possible waves in the different relations described in section 3a. For this purpose, in the following sections 3b and 3c, we use two different wind fields to retrieve two different thermodynamic fields. The first one, referred to as ''a'' is the wind field used in the previous sections. As discussed in Part I, these EVTD-derived fields are obtained through grouping five successive legs together, which represents about three consecutive hours of airborne Doppler data (no changes were made in the time filtering as compared to Part I). The second one, referred to as ''b,'' results from grouping seven successive legs (≈5 h). Figure 10 shows the symmetric tangential wind and the secondary circulation for this ''b'' analysis.

First, the difference between the ''a''- and ''b''-type tangential wind field is the altitude reached by the isotachs. From 1700 to 2200, the maximum altitude of the 40 m s^{-1} isotach decreases from 5.5 to 2 km for the ''b''-type field, and from 5 km to 3 km for the ''a''-type field. Second, the ''b''-type streamfunction differs slightly from

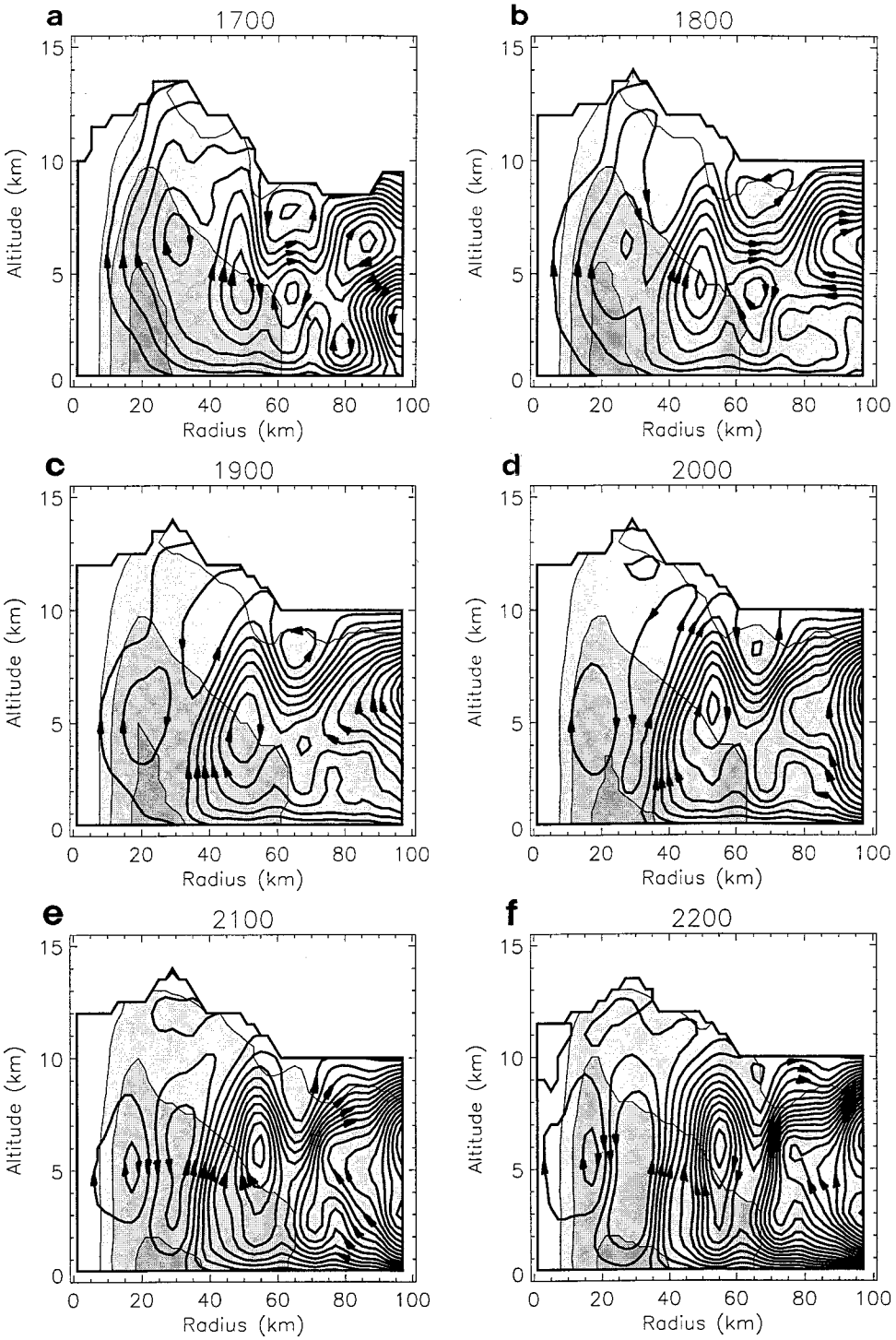

FIG. 10. As Fig. 1 except for "b" analysis.

the "a" one. At 1700 the "b" and "a" secondary circulation are nearly identical, except for a distinct weak clockwise gyre at 50-km radius and 5-km altitude, which does not appear clearly in "a" field. Then, the evolution of "a" and "b" streamfunction is similar, except that in the "b" case, the inner clockwise gyre at 15-km radius does not clearly move upward. For the latest analysis (Fig. 10e), the "b" streamfunction shows two distinct gyres instead of a bigger unique one (Fig. 1e) in the external part of the domain (radius greater than 40 km).

Nevertheless, at 2200 a main updraft at 30- to 50-km radii and a strong inflow in the lower-left part of the domain are visible in both ''a'' and ''b'' fields.

Then the thermodynamic fields are retrieved following the same procedure as described in section 2. As the structure of the ''b'' wind field is not very different from the ''a'' one, Fig. 11 only shows the symmetric temperature perturbation field, θ_{cd0}, derived from ''b'' winds. A comparison between Figs. 2 and 11 reveals similar structures of the temperature perturbation field: a 9-K warm core in the inner part of the eyewall and in the midtroposphere (7–8-km altitude), and a maximum temperature gradient in the eyewall (10–20-km radii). There are, however, important differences in the evolution. The changes in the temperature maximum close to the storm center are much less marked in ''b'' than in ''a.'' Likewise, the cooling observed in the outer part of the domain in ''a'' does not appear in ''b.'' Although less pronounced in ''b'' than in ''a,'' there are, however, some signs of increased warming in the middle part of the domain.

In the following section, we present more quantitative comparisons between the ''a''- and ''b''-type fields in order to determine the influence of time filtering in the balance predicted by the theory through (17), (18), and (19).

c. Balanced structure

The verification of the balanced vortex hypothesis depends on the validity of (17) for the gradient wind balance, (18) for the hydrostatic equilibrium, and (19) for the thermal wind equation. We have estimated how these three equations are verified in the considered domain, for the ''a'' and ''b'' types of analysis. For this purpose, we have computed for (17), (18), and (19), of the form $X = Y$, the rms normalized deviation (RND), as

$$\mathrm{RND} = \frac{1}{N_r N_z}\left[\sum_{i=1}^{N_r N_z} \frac{(X - Y)^2}{\left(\frac{X + Y}{2}\right)^2}\right]^{1/2}, \qquad (20)$$

where N_R is the number of rings and N_Z is the number of levels. The corresponding results are presented, respectively, in Table 2 for (17), Table 3 for (18), and Table 4 for (19).

Table 2 shows the accuracy of the hydrostatic equilibrium hypothesis (18). The RND for the ''a''-type field is 7.7%, slightly larger than that of the ''b''-type field at about 7%. Both of these errors evolve with time, decreasing at 1700 and 1800, and increasing after. The hydrostatic hypothesis (18) is equivalent to considering that the dynamic contribution A_{z0} is small as compared to $g(\theta_{cd0}/\theta_{ve})$. This difference between the ''a'' and ''b'' fields probably come from the stronger time filtering in the later, which substantially decreases the small-scale variation of the horizontal wind and the intensity of the vertical motions.

The RND between both sides of gradient wind equation (17) are presented in Table 3. This equation implies that the symmetric radial pressure gradient $\partial\pi_{d0}/\partial_r$ is mainly controlled by the wavenumber 0 of the tangential speed. We may see that the fit is slightly better for ''b''-type fields (about 7.3%, as compared to 7.7% for ''a''). The RND for ''a''-type fields decreases at 1700 and 1800 and then increases from 1900 to 2200. The ''b''-type error shows a different evolution, decreasing from 1700 to 2100 and then increasing at 2200. This equation is associated with the inertial equilibrium in the system. Similarly, the more filtered ''b''-type fields are characterized by stronger inertial stability.

Finally, Table 4 shows the results obtained for the thermal wind equation (19). Accuracy of this equation (RND is always less than 0.8%) shows the good consistency between the symmetric tangential wind and retrieved temperature. It may be also seen that the ''a''-type fields give slightly better results than the ''b''-type. This shows that, although there are slightly larger differences between the horizontal pressure gradient and the centrifugal acceleration, and between the vertical pressure gradient and the hydrostatic term for ''a'' than for ''b'' analyses, the EVTD-derived tangential wind and the retrieved temperature perturbation are more coherent for the smaller time filtering.

The difference between the two sides of the thermal wind equation $[\beta^2 - (g/\theta_{ve})\partial\theta_{cd0}/\partial r]$ for the ''a'' and ''b''-type fields is shown in Figs. 12 and 13. The global characteristics are similar, with alternation of positive and negative regions. At 1700, for both ''a'' and ''b'' fields, there are two main positive maxima ($+3 \times 10^{-6}$ s^{-2}). The first one is at 2–3-km altitude and 5–30-km radii, the second at about 7–8-km altitude and 30–50-km radii. A negative maximum (-4×10^{-6} s^{-2}) is observed between these two regions at 4–6-km altitude and 5–20-km radii. During the following analyses, the amplitude of the lower positive and of the negative maximum diminishes, while that of the upper positive maximum remains approximately constant.

When comparing Figs. 12 and 13 with Figs. 2 and 10, respectively, it may be seen that there is a correlation between the structure of temperature field (6-K isotherm) and the position of the maxima of the difference $[\beta^2 - (g/\theta_{ve})\partial\theta_{cd0}/\partial r]$. As we may suppose that the symmetric tangential wind is more correct because it is more directly obtained from the radar data, this may reflect locally larger uncertainties in the retrieved temperature field. It is also to be outlined that similar discrepancies appear in the ''a''- and ''b''-type fields, showing that this is independent of time filtering. In the very inner part of the eyewall (5- to 7-km radii) and at the low level (3-km altitude), the positive zone may be due to supergradient winds, as described by Willoughby (1991) in the region where the radial inflow decelerates. Nev-

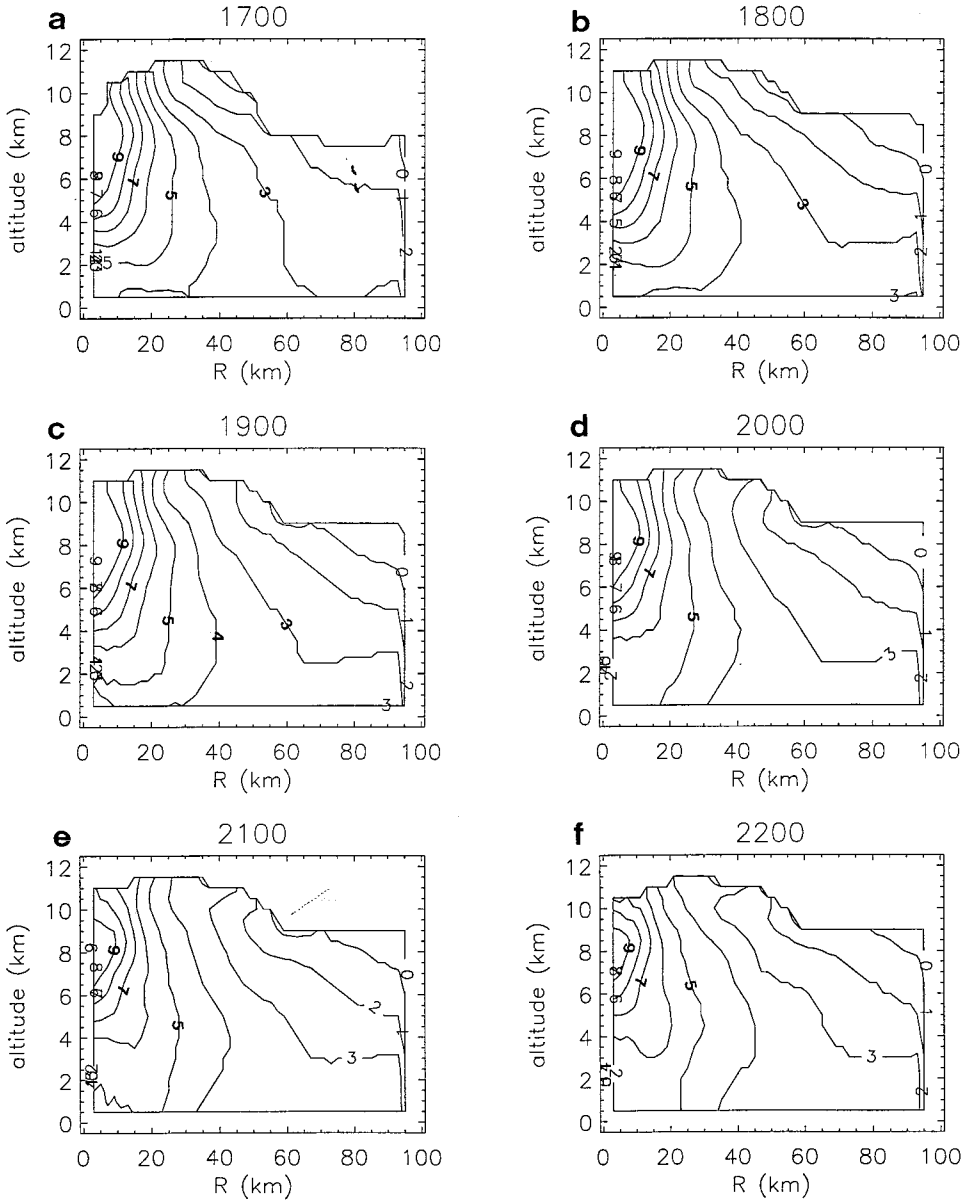

FIG. 11. As Fig. 2 except for "b" analysis.

TABLE 2. Root-mean-square normalized difference (RND) between the two sides of hydrostatic equilibrium equation for the "a"- and "b"-type analyses.

Time (UTC)	Type "a"	Type "b"
1700	7.78×10^{-2}	7.33×10^{-2}
1800	7.60×10^{-2}	7.00×10^{-2}
1900	7.77×10^{-2}	6.96×10^{-2}
2000	7.80×10^{-2}	6.95×10^{-2}
2100	7.84×10^{-2}	6.97×10^{-2}
2200	7.95×10^{-2}	7.01×10^{-2}

TABLE 3. As in Table 2 except for the gradient wind balance equation.

Time (UTC)	Type "a"	Type "b"
1700	7.84×10^{-2}	7.42×10^{-2}
1800	7.69×10^{-2}	7.06×10^{-2}
1900	7.88×10^{-2}	7.04×10^{-2}
2000	7.87×10^{-2}	7.03×10^{-2}
2100	7.94×10^{-2}	7.03×10^{-2}
2200	8.03×10^{-2}	7.08×10^{-2}

TABLE 4. As in Table 2 except for the thermal wind equation.

Time (UTC)	Type "a"	Type "b"
1700	5.34×10^{-3}	5.99×10^{-3}
1800	7.18×10^{-3}	7.62×10^{-3}
1900	5.39×10^{-3}	7.03×10^{-3}
2000	4.34×10^{-3}	7.08×10^{-3}
2100	5.40×10^{-3}	6.43×10^{-3}
2200	6.46×10^{-3}	7.21×10^{-3}

ertheless, the gradient wind balance is globally verified at less than 1% over the whole domain, whatever the time filtering is.

5. Summary and perspectives

The Doppler and reflectivity data collected on 7 September 1991 in Hurricane Claudette with the tail radars of the NOAA WP-3D aircraft were analyzed with the EVTD method as presented in Part I of this paper (Part I). In Part II, we have presented the adaptation of a thermodynamic retrieval method to the EVTD Fourier series expansion. The analysis describes the three com-

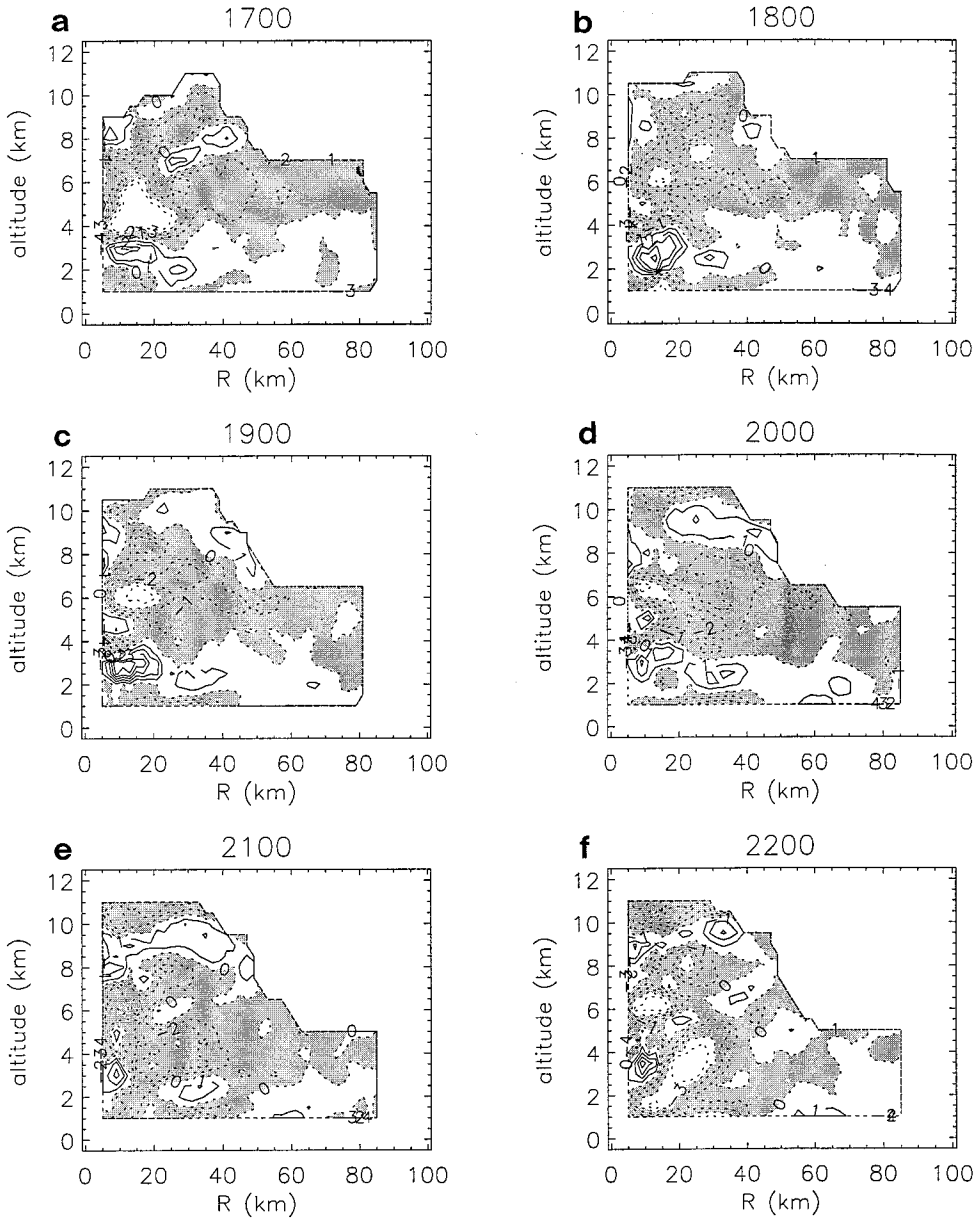

FIG. 12. As Fig. 2 except for the difference between the two sides of the thermal wind equation: $\beta^2 - (g/\theta_{v0})\partial\theta_{c0}/\partial r$, for the "a"-type fields (contour interval is 10^{-6} s^{-2}, shaded zones are for negative values).

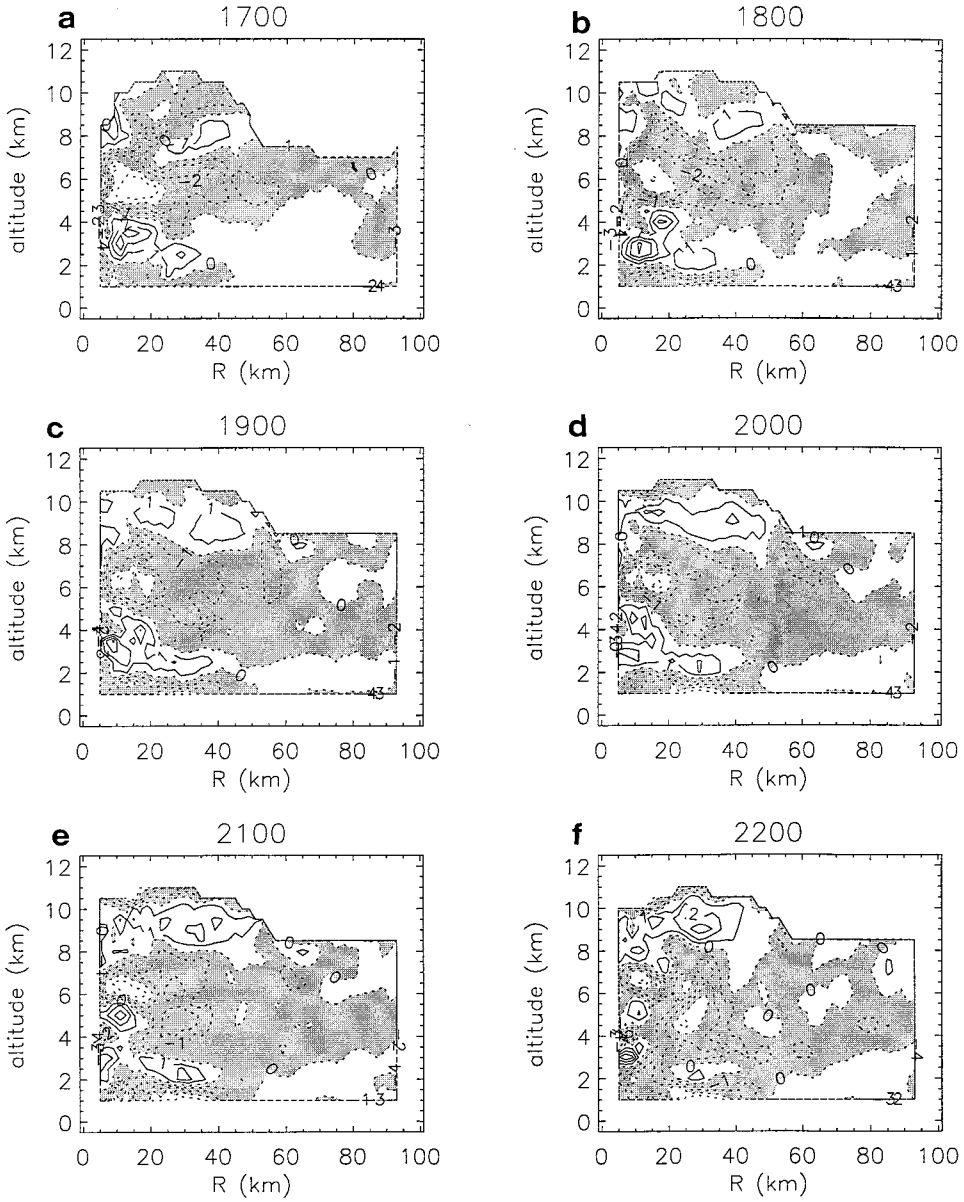

FIG. 13. As for Fig. 12 except for "b"-type fields.

ponents of the wind field, the precipitating water content, and the precipitation terminal fall speed expanded as Fourier series truncated at order 2 in a cylindrical coordinate system. The data are projected onto 50 rings of 2-km width and 25 levels of 500-m depth. The results are obtained for six successive analysis periods at 1700, 1800, 1900, 2000, 2100, and 2200, by interpolation from data collected during the successive legs. The interpolation implies a time filtering, which ensures that the small spatial and temporal scales due to convective and inertial perturbations are eliminated. The only difference between the wind fields in Part I and those utilized here is that an additional constraint is applied to minimize all the wind components at the storm center. The difference between the two sets of wind fields is negligible, except for radii less than 10 km. The retrieved temperature and pressure perturbation fields are also expressed as Fourier series at wavenumber 2, in the same coordinate system, at the same six analysis times.

Comparisons of the retrieved temperature and pressure values with independent in situ data collected along the aircraft trajectories show good qualitative agreement for temperature, although the EVTD-derived fields are smoother than the in situ data. A good agreement is also found for the pressure perturbation, except for some of the circular legs. This probably results from discrepancies in the position of the storm center between the retrieved field and the flight-level data.

These EVTD-derived fields confirm the strong link between kinematic and thermodynamic structures in hurricanes, especially when a partial eyewall replacement cycle occurs. The temperature field evolves as the secondary circulation changes. The inner maximum first increases, then decreases, in agreement with the evolution of the inner eyewall circulation. In the middle and outer part of the domain, the changes in the temperature field are related to the strengthening secondary eyewall and intensifying associated inflow. During the whole period of the analysis, the pressure field does not evolve very much.

Tests were also conducted to estimate how balanced the symmetric vortex is. The symmetric and asymmetric parts of the kinematic and thermodynamic fields can easily be separated owing to the EVTD analysis in terms of Fourier series. Hydrostatic equilibrium, gradient wind balance, and thermal wind equation are tested with two sets of wind, pressure, and temperature fields, in order to check the influence of time filtering. The results show first that hydrostatic equilibrium and gradient wind balance are closely verified (within 8%), and thermal wind relation is even better verified (within 1%,). This implies that inertia–gravity waves and convective motions have been filtered out. Nevertheless, some possible signs of supergradient winds are found in the low levels in the inner part of the eyewall where radial wind decelerates. This may be an artifact resulting from too smooth pressure gradient and tangential wind inside the radius of maximum wind. Comparisons between the ''a'' and ''b'' analyses also showed that too strong a time filtering leads to less balanced wind and temperature fields.

These results allow continuation of this study with the analysis of a diagnostic Sawyer–Eliassen equation (Eliassen 1951) for the secondary symmetric circulation. This equation links the heat and momentum fluxes with the evolution of the radial and vertical velocities (Shapiro and Willoughby 1982). Such results will be presented in a forthcoming Part III.

Acknowledgments. We are indebted to R. Burpee and H. Willoughby (Hurricane Research Division, NOAA/AOML, Miami, FL) for permitting analysis of this dataset in CETP. Discussions with F. Marks, H. Willoughby, and L. Shapiro (from HRD) greatly helped to clarify our views on the dynamics of tropical cyclones. We thank the anonymous reviewers for their helpful comments. The NOAA Aircraft Operations Center staff must also be thanked for the excellent job during the 7 September 1991 mission. Support for this study was provided by INSU/PATOM Grants 92/16, 93/20, and 95/01.

REFERENCES

Cressman, G. W., 1959: An operational objective analysis system. *Mon. Wea. Rev.,* **87,** 367–374.

Eliassen, A., 1951: Slow thermally or frictionally controlled meridional circulation in a circular vortex. *Astrophys. Norv.,* **5,** 19–60.

Gamache, J. F., R. A. Houze Jr., and F. D. Marks Jr., 1993: Dual-aircraft investigation of the inner core of Hurricane Norbert. Part III: Water budget. *J. Atmos. Sci.,* **50,** 3221–3242.

Hawkins, H. F., and D. T. Rubsam, 1968: Hurricane Hilda (1964). II. Structure and budgets of the hurricane on October 1, 1964. *Mon. Wea. Rev.,* **96,** 617–636.

——, and S. M. Imbembo, 1976: The structure of a small, intense hurricane—Inez 1966. *Mon. Wea. Rev.,* **104,** 418–442.

Jordan, C. L., 1958: The thermal structure of tropical cyclones. *Geophysica,* **6,** 281–297.

——, and E. S. Jordan, 1954: On the mean thermal structure of tropical cyclones. *J. Meteor.,* **11,** 440–448.

LaSeur, N. E., and H. F. Hawkins, 1963: An analysis of hurricane Cleo (1958) based on data from research reconnaissance aircraft. *Mon. Wea. Rev.,* **91,** 694–709.

Leary, C. A., and R. A. Houze Jr, 1979: Melting and evaporation of hydrometeors in precipitation from the anvil clouds of deep tropical convection. *J. Atmos. Sci.,* **36,** 669–679.

Roux, F., 1985: Retrieval of thermodynamic fields from multiple-Doppler radar data using the equations of motion and thermodynamic equation. *Mon. Wea. Rev.,* **113,** 2142–2157.

——, and N. Viltard, 1995: Structure and evolution of Hurricane Claudette on 7 September 1991 from airborne Doppler radar observations. Part I: Kinematics. *Mon. Wea. Rev.,* **123,** 2611–2639.

——, and F. D. Marks, 1996: Extended velocity track display (EVTD): An improved processing method for Doppler radar observations of tropical cyclones. *J. Atmos. Oceanic Technol.,* **13,** 875–899.

——, V. Marécal, and D. Hauser, 1993: The narrow cold-frontal rainband observed on 12–13 January 1988 during the MFDP/FRONTS 87 experiment. Part I: Kinematics and thermodynamics. *J. Atmos. Sci.,* **50,** 951–974.

Shapiro, L. J., and H. E. Willoughby, 1982: The response of balanced hurricanes to local sources of heat and momentum. *J. Atmos. Sci.,* **39,** 379–394.

Smagorinski, J., 1963: General circulation experiments with the primitive equations. 1: The basic experiment. *Mon. Wea. Rev.,* **91,** 99–164.

Willoughby, H. E., 1977: Inertia-buoyancy waves in hurricanes. *J. Atmos. Sci.,* **34,** 1028–1039.

——, 1990a: Temporal changes of the primary circulation in tropical cyclones. *J. Atmos. Sci.,* **47,** 242–264.

——, 1990b: Gradient balance in tropical cyclones. *J. Atmos. Sci.,* **47,** 265–274.

——, 1991: Reply. *J. Atmos. Sci.,* **48,** 1209–1212.

——, J. A. Clos, and M. G. Shoreibah, 1982: Concentric eye walls, secondary wind maximum, and the evolution of the hurricane vortex. *J. Atmos. Sci.,* **39,** 395–411.